Compressive performance and deterioration mechanism of ultra-high performance concrete with coarse aggregates under and after heating

Congcong Xue [1], Min Yu [1,*], Haoming Xu [1], Lihua Xu [1], Mohamed Saafi [2], Jianqiao Ye [2]

[1]School of Civil Engineering, Wuhan University, Wuhan 430072, China.
[2]School of Engineering, Lancaster University, Lancaster, LA1 4YR. UK.

Abstract: This paper studies the macro compressive strength, morphological changes and microstructure of ultra-high performance concrete (UHPC) with coarse aggregates (CA-UHPC) when they are either exposed to high temperature (hot state) or after exposing to high temperature and cooling to room temperature (cold state). CA-UHPC specimens with a range of coarse aggregates ratios and subjected to temperatures up to 900 °C are tested and evaluated. The compressive test results show that adding coarse aggregates (volume content $\leqslant$30%) can improve compressive strength of CA-UHPC at both room and high temperature. From the test results, strength reduction coefficients of the CA-UHPC of the hot and cold states are proposed, respectively. The paper also presents the results on the micro scale analyses of mass loss, structure morphology, phase transformation and pore evolution of the CA-UHPC after exposed to high temperature, from which the temperature correlations between the evolution of the microstructure of the material, the change of macroscopic strength, and the deterioration mechanism of the materials are discussed.

Keywords: UHPC; coarse aggregates; compressive strength; post and exposed to high temperature; microstructure; deterioration

1 Introduction

Concrete is a widely used building material. It is estimated that the demand for concrete will increase to 18 billion tons by 2050.[1] Compared with traditional concrete, ultra-high performance concrete has more excellent mechanical properties and durability.[2-6]. UHPC usually has a low water-binder ratio (0.16-0.2) and is made of high efficiency water reducer agent, a certain amount of cement and refined silica fume, high-strength and high-durable aggregates and steel fibers.[7] Finer reactive powder and extremely low water binder ratio reduces shrinkage and initial defects, which improves the corrosion resistance and permeability of UHPC. Steel fibers and coarse aggregates improves, respectively, ductility and shrinkage resistance [8] and reduces project cost[9, 10]. Therefore, less materials can be used to achieve better results and reduce maintenance cost and carbon emission. CA-UHPC can be used not only in load-bearing and decorative structure of buildings in civil engineering, but also as high wear-resistant mold in mechanical engineering[11]. As CA-UHPC has been increasingly used world widely[12-14], and in a range of engineering sectors, fire performance of the material is one of the areas that require immediate attention, as high temperature may cause irreversible physicochemical changes and degradation of mechanical properties of the material and fire failure of building structure[15-17], resulting in irreparable losses.

There have been many researches on the post-fire mechanical properties of normal cement-based materials. These researches mainly focused on the residual mechanical properties of the materials, parametric sensitivity analysis and predictive formulas for the post fire mechanical properties.[18-21] Varona et al.[22] studied the residual compressive, tensile, flexural strength and the elastic modulus of fiber reinforced ordinary and high-strength concrete after high temperature, and presented design formulas of compressive and flexural strength. Tai et al.[23] compared the color change and appearance characteristics of reactive powder concrete (RPC) from the room temperature to 800 °C, and developed a regression equation between residual compressive strength and temperature. Zheng et al.[24-27] tested the residual compressive strength, flexural strength and tensile strength of

Corresponding author: ceyumin@whu.edu.cn (M. Yu)

RPC after high temperature and the influence of steel fiber content, and established a relation between residual strength and heating temperature. Hou et al.[28-30] summarized the high-temperature mechanical properties of RPC, and compared the strength change of cubic RPC at high temperature and after cooling. Sanchayan et al.[31] conducted tests on the residual compressive strength, elastic modulus and ultrasonic wave velocity of hybrid fiber reinforced RPC after high temperature, and found the residual strength steadily increased up to 300 °C, then decreased sharply.

To the authors' best knowledge, research on properties of CA-UHPC materials under high temperature or fire, such as high-temperature macro and micro mechanical properties and fire response, etc., are still limited. Siemon et al.[32] studied the compressive strength of CA-UHPC under high temperatures from 20 °C to 800 °C. Banerji and Kodur[33] studied the hot-state mechanical properties of CA-UHPC at temperatures ranging from 20 °C to 750 °C. The above research objects are all UHPC with a coarse aggregate content, which did not show the effect of coarse aggregate content on the macro mechanical properties, nor could reveal the role of coarse aggregates on the micro degradation mechanism of CA-UHPC. In addition, many other factors affecting the mechanical properties of CA-UHPC at high temperature have been studied, mainly including, e.g., fibers, reactive powder, water, admixture, temperature history and maximum temperature, etc., which are closely associated with the macroscopic mechanical properties and microstructure of the materials. Ahmad et al.[34] studied the effects of exposure time and steel fiber content of UHPC on the mechanical properties at 300 °C. The results showed that a 5 hours exposure to 300 °C increased the compressive strength and toughness modulus, but decreased the elastic modulus and flexural strength. The relationship between mechanical properties, steel fiber content and exposure time was established. Banerji and Kodur[33] evaluated the influence of temperature on the mechanical properties of UHPC, and found that compared to conventional concrete, the compressive strength and elastic modulus of UHPC decreased more quickly than the tensile strength and ductility did. Finally, the relationship between the mechanical properties of UHPC and temperature was also formulated.

In order to study the macro mechanical properties of UHPC at high temperature, microstructural analyses are usually carried out with the help of mesoscale tests.[35-38] Kim et al [36] observed the change of pore structure and cracks of cement paste caused by fire. The initial crack at 600 °C most commonly originated at the edge, and network cracks started to form at 900 °C. Lee et al. [37] studied the microstructure and chemical changes such as weight, phase and pore of calcium aluminate cement (CAC) -based UHPC after high temperatures, and concluded that CAC can improve the pore constructure and high temperature resistance, which reduced the strength loss of CAC-based UHPC after high temperature. Seo et al [38] investigated the evolution of microstructure and the mechanical properties of fly ash at high temperature, shown that the pore structure of the samples with high aerogel content hardly changed at high temperature and was similar to the pore structure at room temperature. Canbaz[39] carried out a meso scale study and found that the strength of RPC with different fiber ratios increased first and decreased at 400 °C. Using SEM, Hussein et al[40, 41] found a number of cracks that were caused by thermal expansion and melting of the polypropylene fibers in the RPC after exposure to elevated temperatures. Baharuddin et al[42] also concluded that the internal mechanism of fire-damaged concrete was closely related to the range of high temperature.

Evidently, a better understanding of the mechanical properties of CA-UHPC under and after high temperature is crucial for a reliable pre-fire prevention design and also an effective post-fire structural assessment, repair and retrofitting. Therefore, this investigation aims to study the compressive mechanical properties of four CA-UHPC (with 0, 10%, 20% and 30% of coarse aggregates, respectively) during the course of heating and after heating. The effects of temperature, coarse aggregate content, sample shape and other factors on the material properties are systematically investigated. Thermogravimetric analysis (TGA), morphology analysis, element and phase analysis and pore analysis are used to study property degradation of the materials under high-temperature, their strength reduction under and after heating and the relationship between macro strength and microstructure.

2 Experimental program

2.1 Raw materials and mix proportion

The reactive powder is made of Portland cement, silica fume and fly ash, the chemical compositions of which, as shown in Table 1, are identified by using an X-ray fluorescence spectrometer. The grade of the Portland cement is 52.5. The average particle size and the specific surface area of silica fume is 0.2 μm and 15000~25000 m^2/kg, respectively, which can reduce the porosity of the CA-UHPC. The Grade Ⅰ fly ash is gray white in colour with a fineness of 9%, which can improve the workability of the CA-UHPC mixture. The fine aggregates are quartz sand of 40~70 mesh. The used quartz sand is tested with bulk density of 1.75 t/m^3 and more than 98% silicon dioxide. Since basalt concrete is superior to other silica concrete, artificial basalt is used as the coarse aggregates.[43] The basalt surface is rough and the particle size is 5 mm to 10 mm. The particle size distributions of various raw materials are shown in Fig.1. The length and diameter ratio of the straight copper-plated microfilament steel fiber is about 60, as shown in Table 2. The fibers are to resist early-age self-shrinkage, restrain crack propagation at high temperature and improve strength of the CA-UHPC. The high thermal conductivity of the steel fibers also helps to balance the temperature gradient inside the material at high temperature, thereby improving the burst resistance of the CA-UHPC[44]. The liquid polycarboxylic high-performance water reducer can reach a reduce rate of 37%. UHPC is designed based on densified particle packing. The water binder ratio of all the mix proportions is 0.16, the sand is 1.37 times the cementitious materials in weight, and the volume content of steel fibers is fixed at 2%. According to the existing research and a large number of repeated tests, coarse aggregates with a volume fraction not exceeding 30% increased the compressive strength of CA-UHPC, while coarse aggregates with a volume fraction exceeding 30% reduced the compressive strength. [6, 45-48] Therefore, the volume fraction of coarse aggregates of CA-UHPC is designed to be 0, 10%, 20% and 30%, respectively. Coarse aggregates are added by replacing the same volume of UHPC. Table 3 shows the detailed specifications of the mixtures. The first column listed in Table 3 is the sample number, and A20 is a sample with 20% volume fraction of coarse aggregates, as also shown in the parentheses of the ninth column. The last two columns list the ambient cubic and prismatic compressive strength (f_{cu} and f_c) of the samples, respectively. The minimum compressive strength specified is not less than 120 MPa.[49-54] The mechanical property tests show that the minimum compressive strength of CA-UHPC cube is 121.9 MPa, which agrees well with GB/T 31387-2015 and T/CECS 10107-2020.[51, 52]

Table 1 Composition of reactive powder

Ingredient (%)	CaO	SiO_2	Al_2O_3	Fe_2O_3	K_2O	MgO	Na_2O	SO_3	P_2O_5	MnO	ZnO	SrO
Portland cement	64.94	19.58	4.5	3.119	0.75	2.64	0.079	2.14	0.128	0.127	0.024	0.148
Silica fume	0.213	92.87	0.354	0.113	0.332	0.224	0.068	1.26	0.11	0.008	0.019	0.005
Fly ash	2.44	48.74	30.63	2.611	1.25	0.575	0.552	0.706	0.247	0.016	0.013	0.06

Table 2 Property of steel fibers

Diameter(μm)	Length(mm)	Aspect ratio	Tensile strength (MPa)	Elastic modulus (GPa)	Density(kg/m^3)
200	12	60	3000	200	7850

Table 3 Mixing proportion of CA-UHPC (kg/m^3)

Mixture ID	Cement	Silica fume	Fly ash	Water	Water reducer	Quartz sand	Steel fibers	Coarse aggregates	f_{cu} (MPa)	f_c (MPa)
A0	703.6	131.9	44.0	140.7	26.4	1205.0	158.3	0.0 (0)	121.9	102
A10	630.1	118.1	39.4	126.0	23.6	1079.0	141.8	252.0 (10%)	130.6	107.9
A20	557.2	104.5	34.8	111.4	20.9	954.2	125.4	501.5 (20%)	143.3	111.3
A30	485.6	91.1	30.4	97.1	18.2	831.7	109.3	746.7 (30%)	157.1	119.8

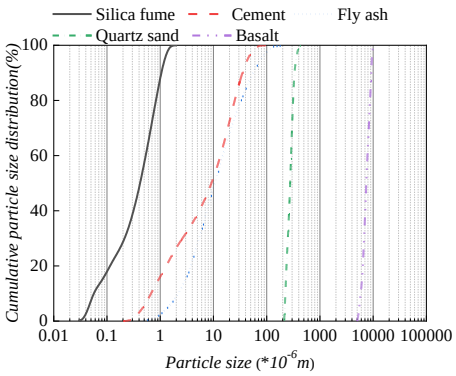

Fig. 1 Particle size distributions of raw materials[48]

2.2 Material and sample preparation

The coarse and fine aggregates were mixed evenly first before adding the reactive powder. Diluted water reducer was added twice to make sure that the aggregates were evenly coated with the cement slurry. Finally, steel fibers were added through a sieve to avoid agglomeration (Fig.2(a)), according to GB/T 31387-2015.[51] Slump tests were carried out to measure the consistency of the mixture and the measurements of the fresh CA-UHPC were between 220 mm to 320 mm (Fig.2 (b) and (c)).[55] To prepare the specimens for testing, the CA-UHPC mixture was poured into the mold that was coated with oily release agent, and covered with film. The hardened CA-UHPC were demolded after 24 hours and then submerged in water for 60 days before they were taken out and placed in a dry and ventilated environment (Fig.2 (d)). The manufacturing process of the samples is shown in Fig.2.

(a) Raw materials (b) Fresh UHPC (c) Slump test (d) Curing sample

Fig. 2 Manufacturing process of samples

2.3 Experimental Tests

2.3.1 Heating process

Considering the thermal resistance of the CA-UHPC, the real-time furnace temperature does not necessarily represent the center temperature of the sample.[4, 56, 57] Therefore, the time required for the sample to reach the required temperature is evaluated. After the furnace temperature has reached 100 °C, 500 °C and 900 °C,

respectively, and kept constant for 1 h ~ 5 h, the measured center temperature of the sample is shown in Table 4. It can be seen that a shorter time is required to reach a higher target temperature as the temperature gradient is higher. In order to reduce burst of the CA-UHPC in the explosive temperature range (200 °C ~ 400 °C), a low heating rate (1 °C / min) is followed and extra one hour of constant temperature at 200 °C, 300 °C and 400 °C is maintained. At the same time, considering the time cost of the test, the duration of heating is set to 3 h and 1 h, respectively, for temperatures below and above 500 °C, as shown in Fig.3. After that, the sample is naturally cooled to room temperature in the furnace.

Table 4 Temperature and duration of heating

Temperature	1 h	2 h	3 h	4 h	5 h
100 °C	71 °C	83 °C	88 °C	90 °C	91 °C
500 °C	480 °C	495 °C	495 °C	495 °C	495 °C
900 °C	882 °C	891 °C	891 °C	891 °C	891 °C

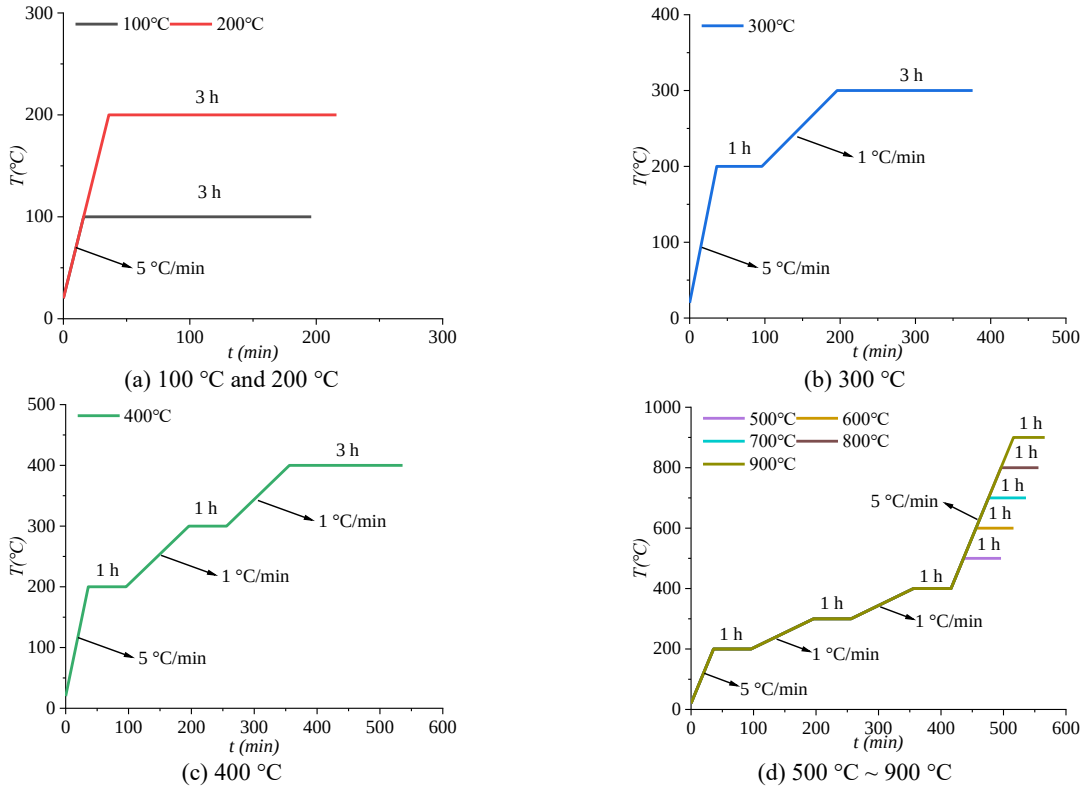

(a) 100 °C and 200 °C (b) 300 °C (c) 400 °C (d) 500 °C ~ 900 °C

Fig. 3 Heating mode of the furnace

2.3.2 Compressive strength test

Three cubic samples of 100 mm and three prismatic samples of 100 mm×100 mm×300 mm were tested for compressive strength. The post-heating strength of the cubes were measured after they had reached their respective target temperature and cooled down to room temperature. The ten target temperatures include room temperature and the temperature from 100 °C to 900 °C of 100 °C interval. The post-heating strength of the prismatic samples and the strength of all the samples under heating were measured at room temperature and the temperatures from 100 °C to 900 °C of 200 °C interval. In total, 336 samples, as shown in Table 5, were manufactured and tested, where C, P, F and U in the ID column denote, respectively, cube, prism, after heating and under heating. For the strength tests under heating, the sample first was fixed in the middle of the press and electric furnace, heated to the target temperature, and then loaded until it was failure. The sample remained in the target temperature from loading to failure. The test instruments are shown in Fig.4.

Table 5 Sample design for compressive strength test

Type of test	ID	Size/mm	Number of mixture (Table 3)	Number of temperature level	Repeated number	Number of sample

Post-heating strength	CF	100×100×100	4	10	3	120
	PF	100×100×300	4	6	3	72
Strength under heating	CU	100×100×100	4	6	3	72
	PU	100×100×300	4	6	3	72

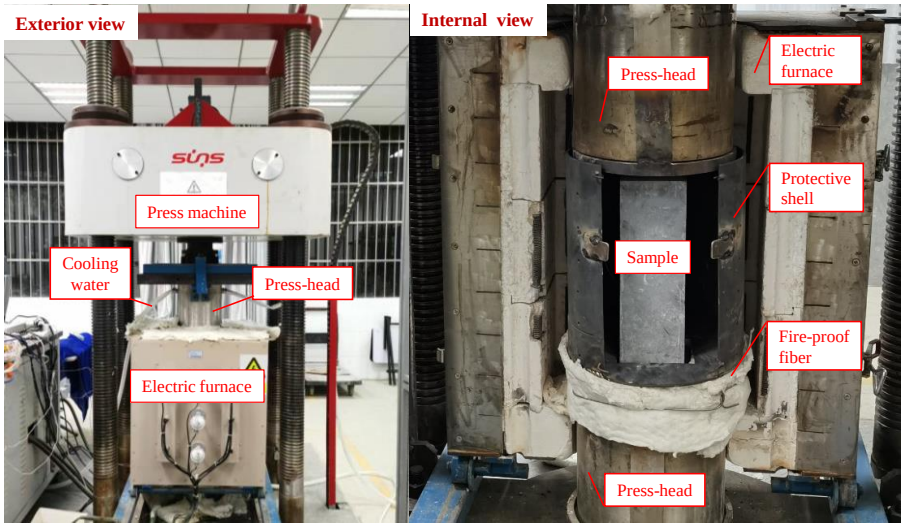

Fig. 4 Test instruments used for strength tests

2.3.3 Microscopy test

Microscopic examination of the CA-UHPC were carried out to study the change of macrostructures before and after heating, including the changes of mass, micro morphology, phase and pore after being heated with different temperatures. Randomly selected material samples were examined by SEM, energy dispersive spectroscopy (EDS) and mercury intrusion porosimetry (MIP). Mortar was ground for TGA and X-ray diffraction analysis (XRD). Samples were also taken from the prisms for X-ray computed tomography (X-CT).

3 Compressive strength at high temperature

3.1 Visual observation and failure mode

3.1.1 Visual observation

Table 6 Morphological changes and physicochemical process of CA-UHPC after high temperature

T(≤)	Sample	Color and knocking sound	Surface appearance	Physicochemical reaction
20 °C ~300°C		Dark gray ~ grey; clear and loud	Smooth surface with small diameter and quantity pores, dense structure.	Loss of free water, rehydration, partial loss of bound water of CSH.
400°C ~500°C		Paler gray; a little dull	Relatively smooth surface with coarse pores, relatively dense structure.	Loss of all physically bond water，decomposition of CSH.
600°C ~700°C		Yellowish-white; dull	Roughened surface with large diameter pores, some loose structure.	The peak of CH decomposition rate, transformation of quartz.
800°C ~900°C		Pink; dull and low	Rougher surface, larger diameter pores, fine cracks and crisp corners, more loose structure.	Decarbonation of calcium carbonate, loss of all chemically bund water.

Note: CH and CSH refer to the abbreviation of calcium hydroxide and hydrated calcium silicate, respectively.

The color change of the CA-UHPC after high temperature is related to the maximum temperature exposed and the change of mechanical properties.[44, 58, 59] The reactive powder, aggregates and steel fibers in the concrete cause permanent color change (Table 6). The color series is roughly summarized as follows: the color of the CA-UHPC at room temperature is dark gray (Fig.2), gray at about 300 °C, paler gray at 400 °C ~ 500 °C, yellowish

white at 600 °C ~ 700 °C, and pink at 800 °C~900°C.

The surface of the sample heated lower than 300°C has numerous small pores, clear and loud knocking sound and no visible cracks,[7, 60] which means a dense internal structure. Loss of free water and bond water in CSH, and rehydration under steam pressure occur at this stage. With further heating, the pores are coarsened with increased diameter, and a light-colored covering is formed on the surface of the CA-UHPC, which is the CaO formed from the decomposition of CSH. At 400 °C, CA-UHPC loses all physically bound water and free water. At 535 °C, the decomposition rate of CH reaches the maximum, and the quartz changes from α to β at 573 °C.[61] At 650 °C, calcium carbonate ($CaCO_3$) begins decarburization, and then the decomposition of CSH in CA-UHPC reaches another peak[62]; Exceeding 800 °C, all chemically bound water is lost. When the sample was taken out of the electric furnace after 900 °C, a brittle sound was heard and fine lines along the steel fiber contour can be seen on the surface of the sample. The cracks at the corners are enlarged and tend to be crisp. The cement slurry falls off at the corners of the sample, but the integrity is maintained. The knocking sound turns to dull and low, reflecting the increase of pores and cracks inside the cube.

3.1.2 Failure characteristics under compression

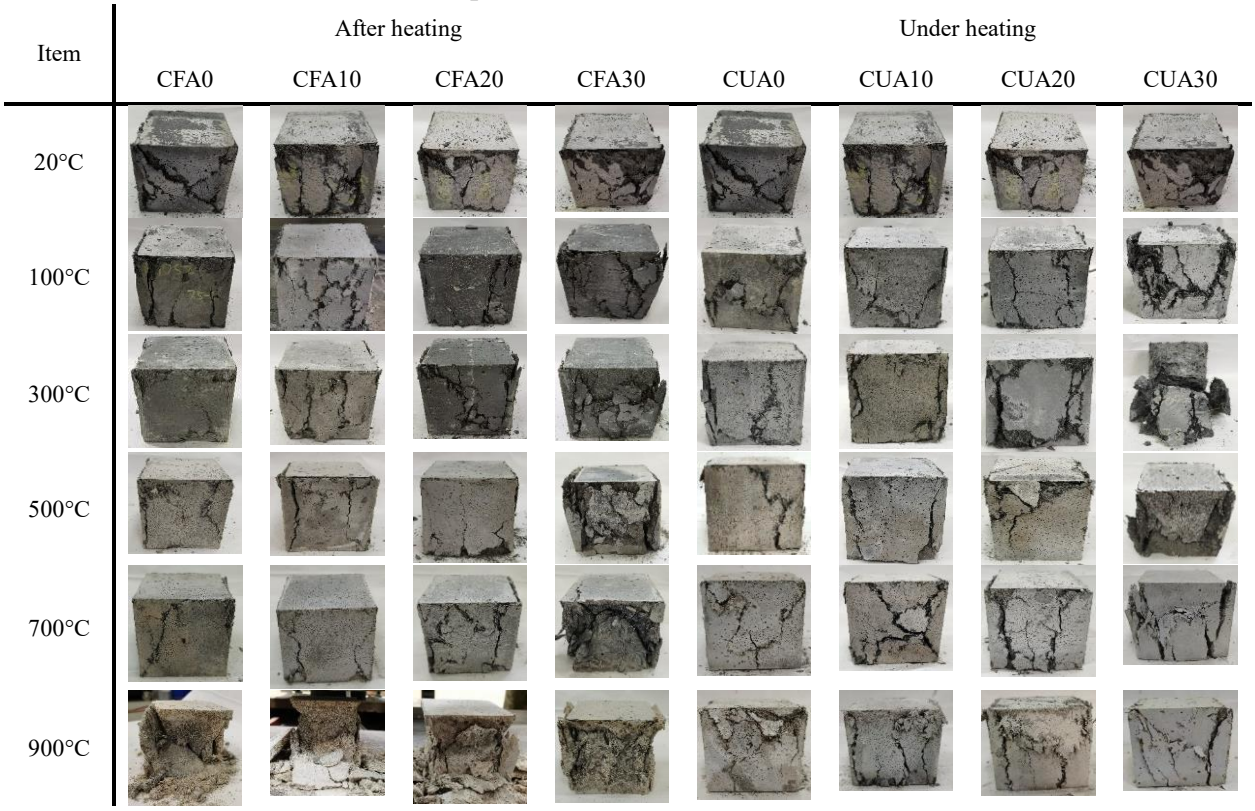

Fig. 5 Compressive failure of samples after and under high temperature

The samples were cooled to room temperature for uniaxial compression test. In the early stage of compression, there were no obvious changes in appearance and sounds. When the load was close to the peak load, sound from steel fibers pulling out was heard. Micro-crack propagated quickly before the final failure. Typical failure modes are shown in Fig. 5. It was found that higher temperature increased the depth of spalling. The failure at a temperature below 500 °C was brittle, evidenced by sudden break and a loud bang.

In general, for the CA-UHPC after and under heating, more coarse aggregate leads to more cracks, and the concrete is more likely to explode. From 300 °C~700 °C, the A30 sample failed with burst fragments of 5mm ~ 100mm long, and, in some cases, bursting of the entire finishing (top) surface of the concrete block occurred. For the samples heated up to a temperature below 700 °C, a close inspection showed dense steel fibers across cracks, i.e. cracks bridging between the opposing fracture surfaces. When a sample was heated above 700 °C, the steel fibers became black due to carbonization, and lost the inhibition effect on the cracks. It was also observed that the failed samples showed little change in shape if they were heated up to temperature below 900 °C. Volume distortion of the samples were obvious when the temperature reached 900 °C, partly due to the

plastic deformation caused by high temperature.

3.2 Studies on compressive strength

3.2.1 Effect of coarse aggregates on the compressive strength under and after high temperature

Three repeated tests were conducted on the samples with the same mixture for the same target temperature, from which the average of the tests was taken. In order to facilitate comparison, the normalized compressive strength, which is defined as the ratio of the compressive strength at temperature T ($f_{cu,T}$ and $f_{c,T}$) to the compressive strength of the same concrete at room temperature ($f_{cu,0}$ and $f_{c,0}$), is plotted in Fig. 6, where $f_{cu,T}$ and $f_{c,T}$ are the compressive strength of the cubic and prismatic samples at temperature T, respectively.

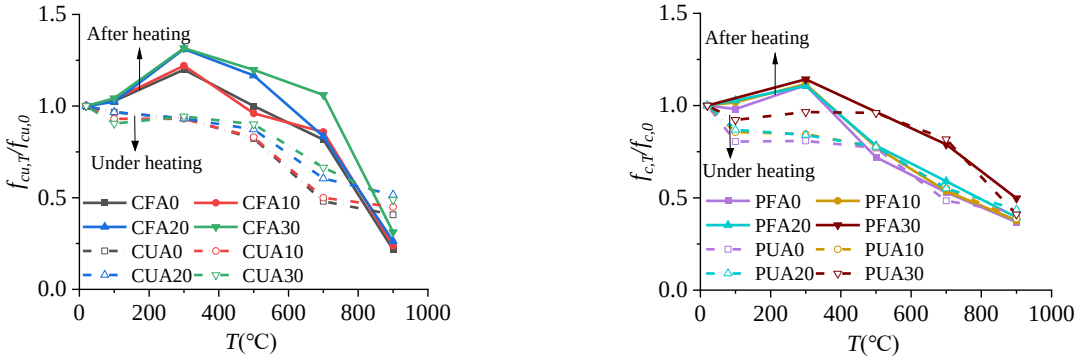

(a) Cube (b) Prism

Fig. 6 Normalized compressive strength of the cubic and prismatic samples

Table 3 shows that the compressive strength of both the cubic and prismatic samples with a higher coarse aggregate content is higher at normal temperature. At normal temperature, the compressive strength of the basalt aggregate is about 180 MPa[63], which is higher than the CA-UHPC matrix. Under compression, the matrix and the coarse aggregates work together, and the coarse aggregates have a blocking effect on the development of cracks. The propagation of micro-cracks usually bypasses coarse aggregates to form a longer failure path, so as to absorb more energy. The same observation from Table 3 is also illustrated in Fig. 6 for the samples subjected to other temperatures, which is attributed to that the matrix has a higher deterioration rate than the coarse aggregates when they are under elevated temperature.

Overall, the post-heating compressive strength of the samples with the same geometry and coarse aggregate content is greater than that when the samples are under the same high temperature. The post-heating strength demonstrates an early increase, followed by a decrease when the temperature increases. Specifically, the post-heating strength increases notably at 300 °C, which is 10% to 20% higher than that of the same concrete at normal temperature. The increase in the post-heating strength can be attributed to the formation of new hydrates in the pores within the material due to the rehydration during evaporation of free water, which brings the cement gel layers move closer to each other, resulting in a larger Van der Waals force[64]. Under 300 °C, the compressive strength is smaller than that at normal temperature. It is speculated that the sample under 300 °C does not go through the long cooling period as the post-heating sample, thus the rehydration reaction time is not long enough to improve the compressive strength.

From 300 °C, the difference between the post-heating strength difference of A30 and the other CA-UHPCs begins to increase until 700 °C. Within this temperature range, the effect of temperature on the rate of deterioration of the matrix is greater than that of coarse aggregates. At 900 °C, the post-heating strength is very low, which is about 40% lower than that at normal temperature. From the test results of all the samples at different temperatures, the compressive strength of A30 is much greater than that of all other CA-UHPCs. It can be judged that adding 0 ~ 30% coarse aggregate can improve the compressive strength of the samples, but the effectiveness is not proportional to the content of coarse aggregates.

3.2.2 Effect of the sample shape on the compressive strength under and after high temperature

It can be seen from Fig. 6 that the normalized compressive strength of the cubic and prismatic samples

follows a relatively similar trend for the samples exposed to and post heating. However, the normalized compressive strength of the cubes is larger than that of the prisms, which means that the strength of the prisms decreases more than that of the cubes when they are subjected to the same temperature. This is partly because the larger volume of the prism that is three times of the cube. Therefore, the prisms are inevitably with more initial damage and prone to high-temperature damage.

To further study the effect of the sample shape, the compressive strength ratio of prismatic and cubic samples is defined as the ratio of the compressive strength of the prisms divided by that of the cubes with the same mixture at the same target temperature. The post-heating compressive strength ratio of CA-UHPC with different aggregate contents is rather similar.

The post-heating compressive strength ratio can be approximately calculated by Eq.(1),

$$\frac{f_{PT}}{f_{CT}} = 3.93\times10^{-4}T + 0.82, \qquad 20°C \le T \le 900°C \tag{1}$$

3.2.3 Prediction of the compressive strength reduction under and after high temperature

The literature review has found that the research on the compressive strength of UHPC are limited, and there are very limited works on the compressive strength of CA-UHPC under and after heating [33][65]. Thus, in this research, compressive strength tests, including post heating (cold state) and under heating (hot state), on UHPC with different coarse aggregate contents are conducted. Due to the lack of existing results for cross examination, the test results of similar concrete, such as RPC[23, 24, 26, 27, 66] without coarse aggregates and ultra-high strength concrete (UHSC) [67-69] with coarse aggregates and fibers, are included in the comparisons, as shown in Fig. 7.

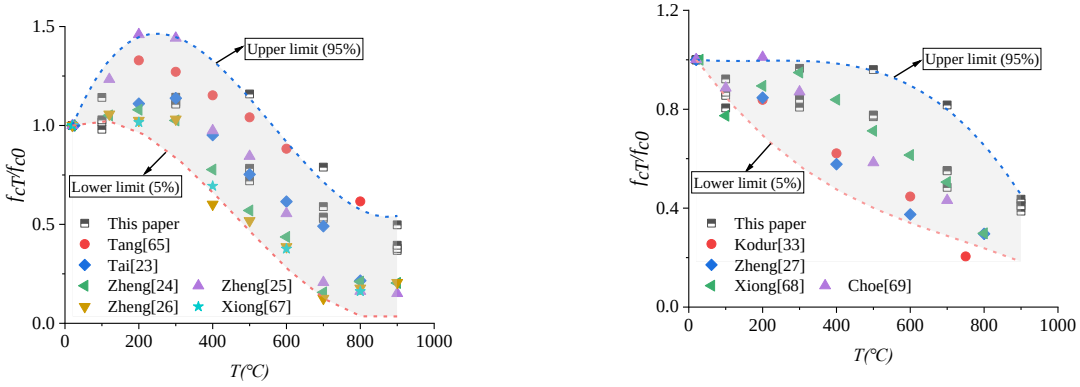

(a) Post heating (cold state) (b) Exposed to heating (hot state)

Fig. 7 Reduction factors of the compressive strength post and exposed to heating

As shown in Fig. 7 (a), the normalized post-heating compressive strength of CA-UHPC, RPC and UHSC all show decreasing after an initial increasing. The difference is that from 500 °C to 900 °C, the CA-UHPC has a higher normalized compressive strength than others. This means that the reduction in the compressive strength of the CA-UHPC within this temperature range is less severe when compared to the other materials. In Fig. 7, cubic polynomials are used to fit both the upper and lower bounds of the normalized compressive strength over the temperature range. It is found that data outside the area enclosed by the upper and lower bounds are about 5% on each side. The normalized compressive strength of the CA-UHPC, i.e., the reduction coefficient of the CA-UHPC, after heating (cold state) is also given by curve fitting the test results.

The upper bound of the normalized post heating compressive strength is,

$$k_{up,F} = 7.58\left(\frac{T-20}{1000}\right)^3 - 12.33\left(\frac{T-20}{1000}\right)^2 + 4.46\frac{T-20}{1000} + 1, \qquad 20°C \le T \le 900°C \tag{2}$$

where F refers to post heating.

The lower bound of the normalized post heating compressive strength is,

$$k_{low,F} = 4.51\left(\frac{T-20}{1000}\right)^3 - 6.11\left(\frac{T-20}{1000}\right)^2 + 0.78\frac{T-20}{1000} + 1, \qquad 20°C \le T \le 900°C \tag{3}$$

The compressive strength reduction coefficient of the CA-UHPC after heating is,

$$k_F = 1.07 - 0.75e^{(-0.5((T-891.43)/247.66)^2 - 0.5((V_A-0.07)/0.24)^2)}, \quad 20°C \le T \le 900°C \tag{4}$$

where, V_A refers to the volume fraction of coarse aggregates.

The simplified reduction coefficient of compressive strength of the CA-UHPC after heating is,

$$k_{S,F} = \begin{cases} 1, & 20°C \le T \le 300°C \\ -9.84\times10^{-4}T + 1.3, & 300°C < T \le 900°C \end{cases} \tag{5}$$

For the materials under heating, as shown in Fig. 7(b), the normalized compressive strength is always smaller than the strength under room temperature, which is different to Fig. 7(a) when the temperature is below 300 °C. As observed in Fig. 7(a), the normalized compressive strength of CA-UHPC under a temperature from 500 °C to 900 °C is also greater than that of the other materials. Similarly, the upper limit bound, the lower limit bound, and the compressive strength reduction coefficient of the CA-UHPC under heating are given as follows (Eq.(6)~Eq.(9)).

The upper bound of the normalized under-heating compressive strength is,

$$k_{up,U} = -1.54(\frac{T-20}{1000})^3 + 0.78(\frac{T-20}{1000})^2 - 0.11\frac{T-20}{1000} + 1, \quad 20°C \le T \le 900°C \tag{6}$$

where, U refers to under-heating.

The lower bound of the normalized under-heating compressive strength is,

$$k_{low,U} = -1.03(\frac{T-20}{1000})^3 + 2.2(\frac{T-20}{1000})^2 - 2.07\frac{T-20}{1000} + 1, \quad 20°C \le T \le 900°C \tag{7}$$

The compressive strength reduction coefficient of the CA-UHPC under heating is,

$$k_U = 0.92 - 6.1\times10^{-7}(T-20)^2 - 1.04\times10^{-4}(T-20) + 1.97V_A^2 - 0.3V_A + 2.72\times10^{-4}(T-20)V_A, \ 20°C \le T \le 900°C \tag{8}$$

The simplified reduction coefficient of compressive strength of the CA-UHPC under heating is,

$$k_{S,U} = -6.67\times10^{-4}T + 1.01, \quad 20°C < T \le 900°C \tag{9}$$

4 High-temperature micromorphology and composition analysis

4.1 Mass analysis

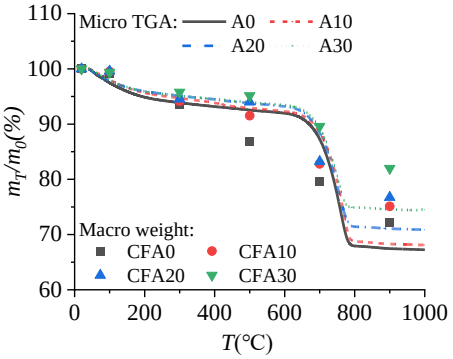

Fig. 8 Macro and micro mass change of CA-UHPC

The mass changes of the micro TGA (Type TGA2) and the macro samples[55] are plotted in Fig. 8. The comparison demonstrates that the mass of the samples decreases with the increase of temperature, and the high temperature causes irreversible changes in the material. Water in the concrete includes free water and bound water. From normal temperature to 300 °C, the mass of the samples is constantly decreasing and the reduction rate is faster, especially at 150 °C. At this time when evaporation of free water occurs, the balance inside the material is broken, resulting in separation and evaporation of the bound water in CSH [70]. The mass loss in this

temperature range is 4.9% ~ 6.1%. The mass decreases by 1.3% ~ 1.9% at 300 °C ~ 500 °C compared with that below 300 °C. The reduction rate is relatively slow in comparison to the previous stage, mainly due to the dehydration of CH starting at 450 °C [71]. After 500 °C, the mass decreases significantly again, because $CaCO_3$ begins to decarburize at 650 °C, resulting in a 4.4% ~ 6.1% reduction in mass at 500 °C ~ 700 °C in contrast with the previous stage. At 700 °C ~ 900 °C, the mass decreases by 14.8% ~ 20.2% that at 500 °C ~ 700 °C, and the reduction rate reaches the maximum at 720 °C, accompanied by solid-solid transformations. The mass decreases most in this temperature range, which corresponds to the decrease of the macro post-heating strength.

Compared with normal temperature, the average macro and micro mass loss at 900 °C is 30.4% and 23.5%, respectively. The mass change of TGA is more evident than that of the macro weighing. It can be attributed to that the samples tested by TGA are powder that have larger specific surface area and decomposed more at high temperature. As for the influence of the coarse aggregate content, both the micro TGA and macro weight show the same law that the more the coarse aggregate content, the less the mass loss.

4.2 Micro morphology analysis

4.2.1 Morphology of the CA-UHPC matrix after different temperatures

The morphology and the qualitative and semi quantitative analysis of the CA-UHPC samples before and after high temperature are examined by SEM (type: Zeiss SIGMA) and EDS. The results are analyzed for the matrix, steel fibers, coarse aggregates and their interfaces, as shown in Fig. 9~Fig. 11.

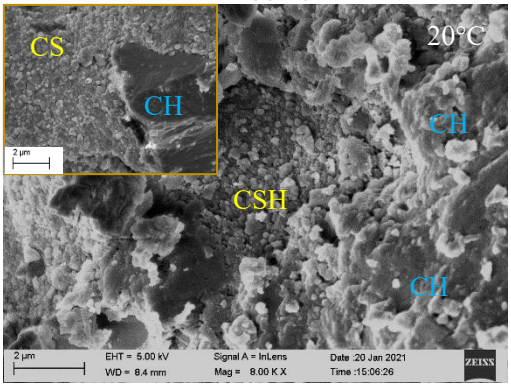

(a)

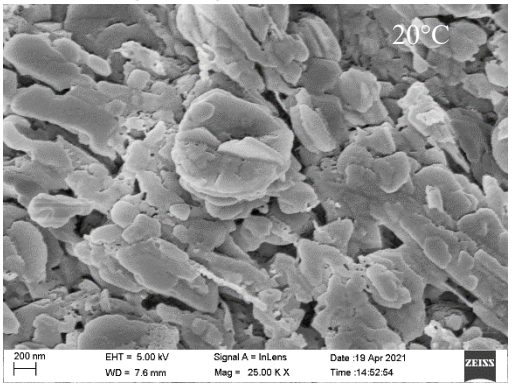

(b)

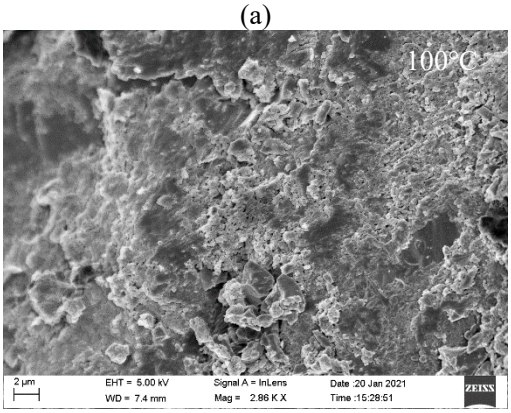

(c)

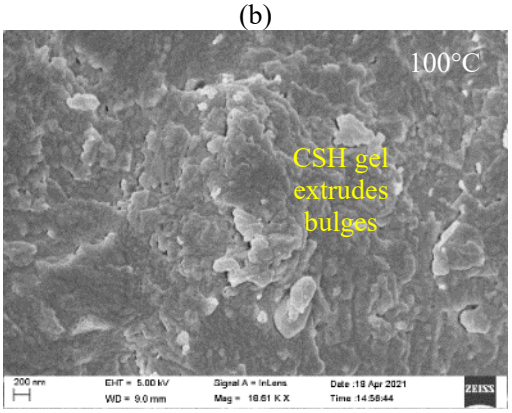

(d)

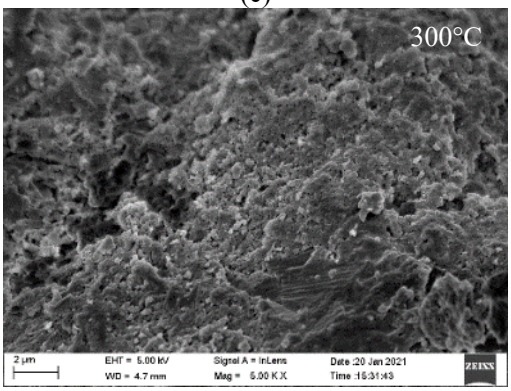

(e)

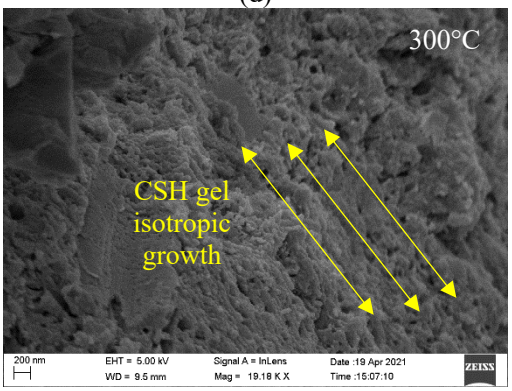

(f)

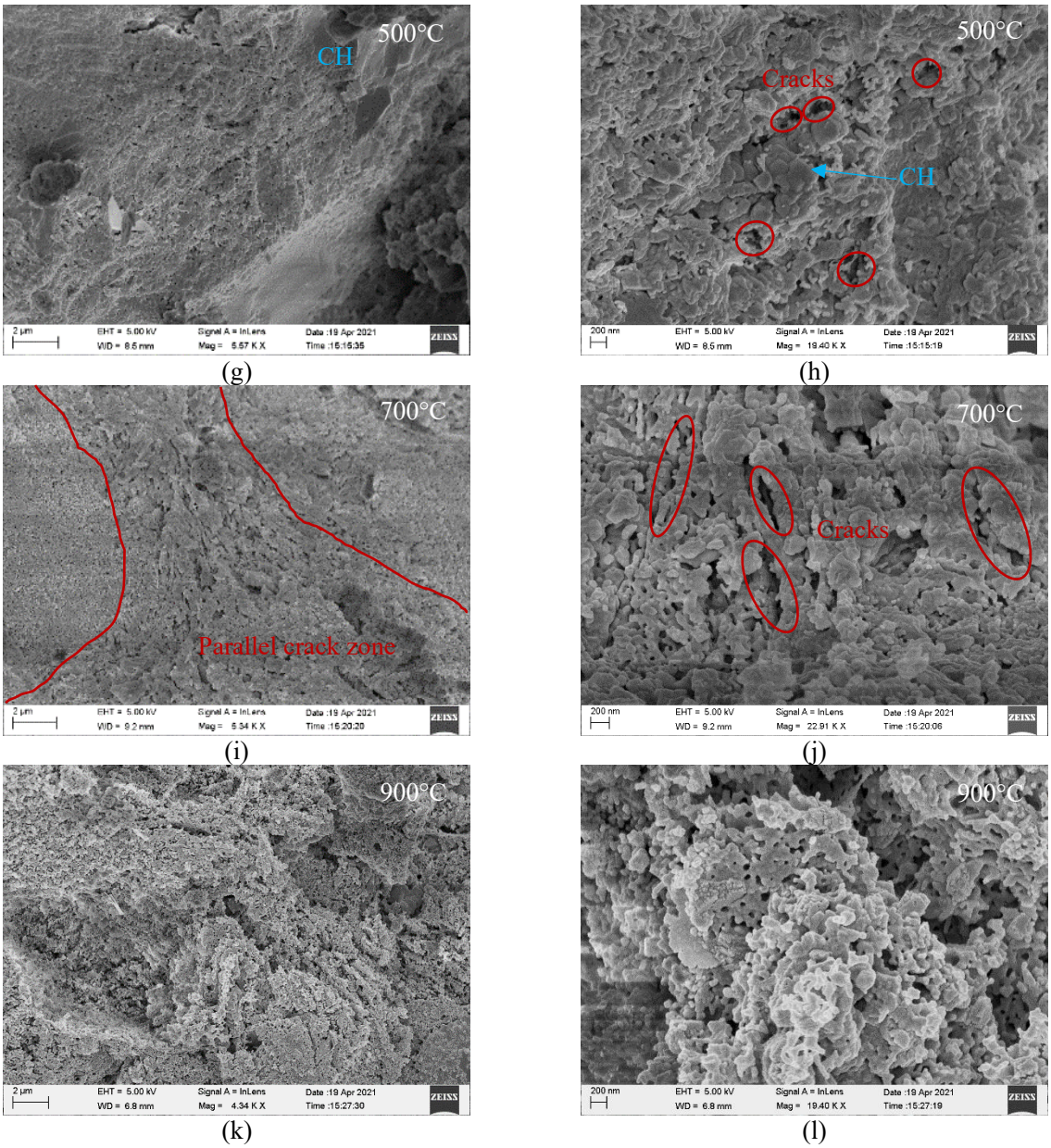

Fig. 9 SEM image of CA-UHPC matrix after high temperature

At room temperature (Fig. 9(a)), the matrix is relatively dense without evident defects, and CSH and CH can be observed. It is because that CSH is a primary hydration product, which presents amorphous CSH gel, and CH presents plate-like structure. They are closely arranged together in a certain form. When it is magnified to 25000 times (Fig. 9(b)), it can be seen clearly that the hydrate structure is straight without bending. However, there are still voids between the structures, which are not filled by hydration. The Ca/ Si ratio measured by EDS is 2.53.

When the temperature rises to 100 °C and 300 °C (Fig. 9(c)~(f)), the matrix is further compacted, and the silicon powder further involves in the hydration reaction. The voids in normal-temperature structure (Fig. 9(b)) are filled with the hydrates, and CSH gel continues to grow and extrudes bulges on the matrix (Fig. 9(d)). At 300 °C, the material inside is denser, the lamellar CSH gel disappears, and CSH of the cluster structure in crowded space finally presents weak co-directional growth (Fig. 9(f)). The Ca/ Si ratio of the matrix at 100 °C and 300 °C are 1.88 and 1.02, respectively, indicating that CSH is generated, CH is consumed and the hydration reaction continues from room temperature to 300 °C. Compared with the structure at 100 °C (Fig. 9(d)), the structure at 300 °C (Fig. 9(f)) has a small number of fine holes, illustrating that there has been preliminary thermal stress damage at 300 °C. However, from the macro mechanical properties (Fig. 6), the strength enhancement caused by rehydration is greater than the strength reduction caused by thermal stress damage.

At 500 °C, the micro structure becomes a little loose, the structure in Fig. 9(g) tends to get chapped. Fig. 9(h) shows a small number of holes and cracks, the hydration products are not dense, and the components are separated with voids. At this time, free water and physical crystal water disappear. At 700 °C, the pore structure is further coarsened, and there are many and concentrated cracks in Fig. 9(i), forming parallel crack zone. In Fig. 9(j), the structure tends to form long cracks, and obvious boundaries and cracks appear between particles. CSH and CH are almost completely decomposed. These long cracks in the parallel crack zone are easy to penetrate each other, resulting in a significant reduction in the macro compressive strength. At 900 °C, the micro structure (Fig. 9(k)) is full of holes and cracks, which are widened and deepened. On magnification (Fig. 9(l)), the cracks are penetrated, the internal skeleton is coral-like, with no compound filling it. Thermal stress makes the structure curl and shrink.

4.2.2 Morphology of steel fibers in CA-UHPC after different temperatures

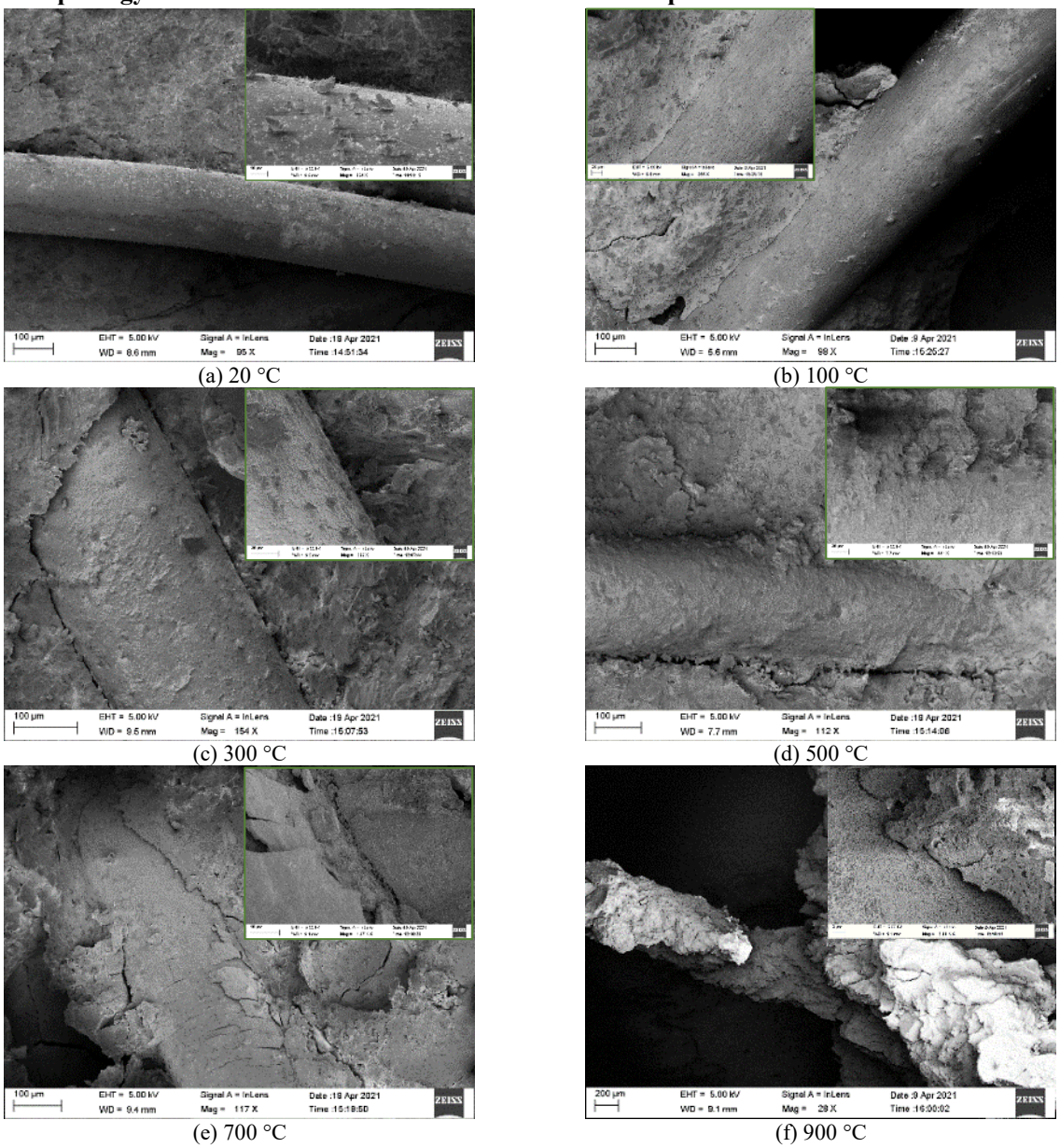

(a) 20 °C (b) 100 °C

(c) 300 °C (d) 500 °C

(e) 700 °C (f) 900 °C

Fig. 10 SEM image of steel fibers in CA-UHPC after high temperature

The surface morphology of the extracted steel fibers is shown in Fig. 10. At room temperature, the surface of the steel fiber is smooth and complete, and almost no matrix is bonded to the surface. After amplification, small particles are observed on the fiber surface. It indicates that the failure occurs at the bonding surface. After 100 °C, the surface of the steel fiber is still smooth, and scratches along the radial direction of the fiber are observed, indicating that the surface of the steel fiber has been bonded to the matrix. This demonstrates that there is a strong adhesion between the fiber and the matrix. After 300 °C, there is thin matrix attached to the surface

of the steel fiber, meaning that the steel fiber is still closely connected with the matrix, and the failure occurs further away from the bonding surface. After 500 °C, the surface of the steel fiber covered with matrix is no longer smooth. There are vertical and parallel cracks between the steel fiber and the matrix. However, the steel fiber remains bonded to the matrix. After 700 °C, the surface of the steel fiber peels and partially detaches. There are many longitudinal cracks between the steel fiber and matrix, which illustrates that the steel fiber has significant damage [72], and the bond between the steel fiber and matrix degrades. After 900 °C, the pulled part of the steel fiber carries thick matrix, and the thickness of the matrix in different parts varies greatly, so the original cylindrical shape of the steel fiber can hardly be distinguished.

As can be seen from the shape of the extracted fiber, the matrix attached to the fiber becomes thick with the increase of temperature, that is, the failure surface changes from the steel fiber-matrix interface to the shallow matrix and even to the deep matrix. On the one hand, it means that within 300 °C, the fiber-matrix interface is enhanced due to re-hydration. On the other hand, as the temperature continues to rise, the matrix deteriorates rapidly, and the bond force between the steel fiber and the surrounding matrix is gradually greater than that inside the matrix.

4.2.3 Morphology of coarse aggregates and holes in CA-UHPC after different temperatures

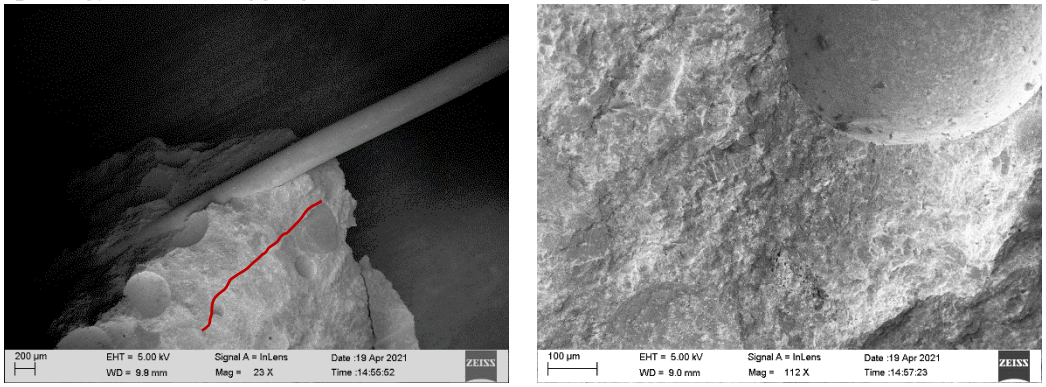

(a) 100 °C

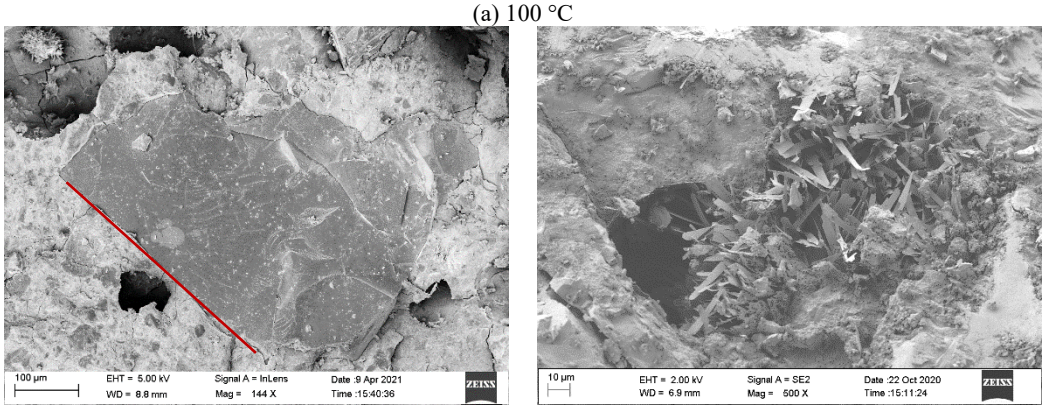

(b) 300 °C

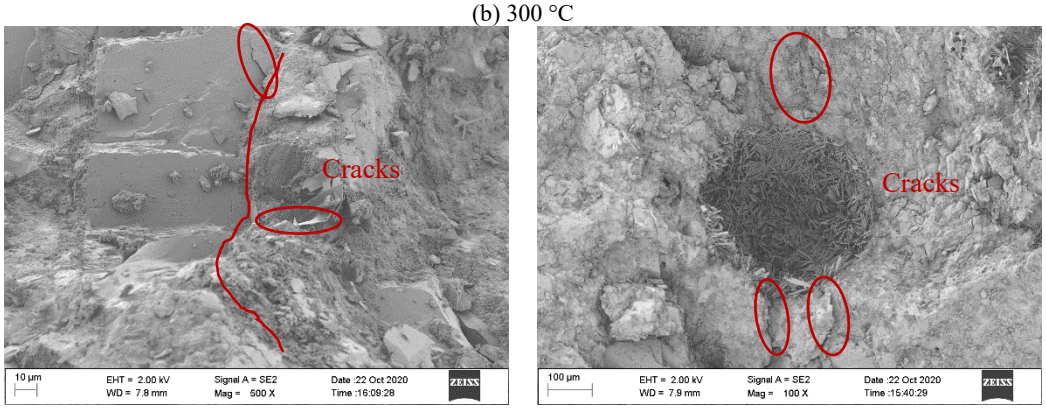

(c) 500 °C

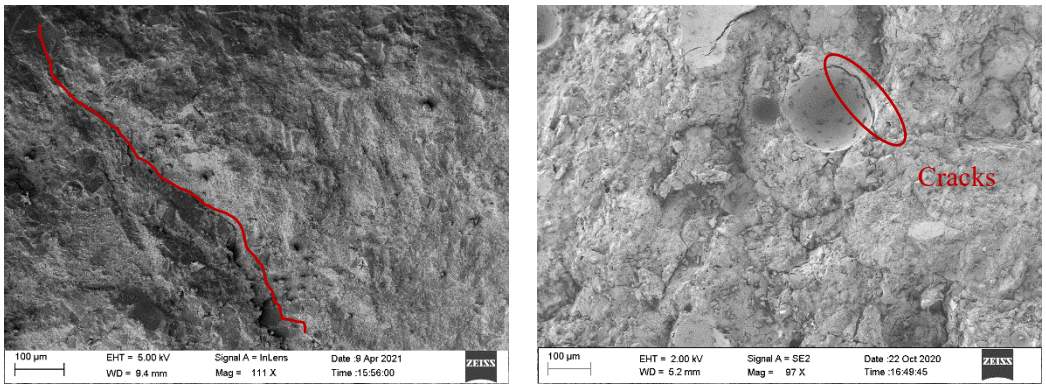

(d) 700 °C

Fig. 11 SEM image of coarse aggregates and pores in CA-UHPC after high temperature

The morphological characteristics of coarse aggregates and holes are shown in Fig. 11. From room temperature to 300 °C, the boundary between the coarse aggregate and matrix is clear and the bond is tight. The internal holes of the CA-UHPC change from smooth inner wall to form a large number of needle-like CSH, which means that the internal hole provides space to generate new CSH under the combined action of temperature and free water. On the sample section after 300 °C (Fig. 11(b)), the coarse aggregate is flat and smooth, like being cut, which may be because the new hydrate enhances the strength of the matrix itself and the matrix-coarse aggregate interface, causing the failure surface pass through the coarse aggregate. After 500 °C, the boundary between the coarse aggregate and matrix is no longer clear. It can be clearly seen that the coarse aggregate has uneven surface, and there are some cracks and radial cracks between the coarse aggregate and the matrix. CSH in the hole decreases and radial cracks appear around the hole. After 700 °C, the surface of the coarse aggregate is covered with the matrix, and the shape of the coarse aggregate occasionally appears, which is difficult to distinguish. There are obvious cracks and no hydrates in the hole.

4.3 Element and phase analysis

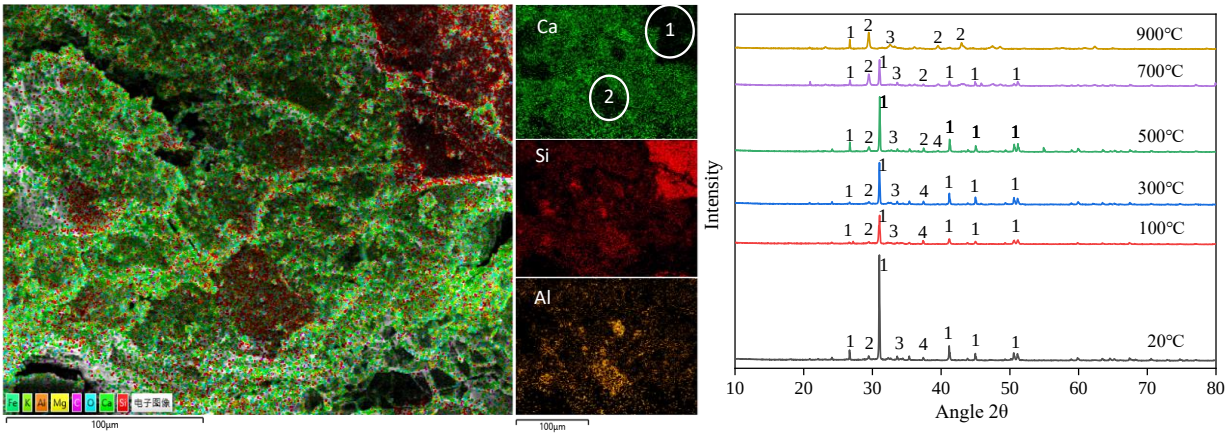

(a) Element distribution map (b) XRD test results

Fig. 12 Elements and phases in CA-UHPC

The element diagram of the CA-UHPC at room temperature (Fig. 12(a)) was collected by EDS. The main elements Ca, Si and Al are evenly distributed on the surface of the sample. Ca element diagram is dark in area ① of the upper right conner and area ② of the middle. Corresponding to area ①, Si element appears very bright due to the embedding of the aggregate. Corresponding to area ②, Al element appears very bright due to the formation of calcium aluminate hydrate. Except for areas ① and ②, there is no element enrichment in the distribution map of Ca, Si, Al and other elements, and the hydration products are also evenly distributed. On the whole, the microstructure of the CA-UHPC is uniform, the different components are closely combined, and the initial defects are small.

Combined with the EDS of the sample, it can be seen that the elements in the matrix are mainly O, Ca, Mg, C, Al, Si, K etc., so as to accurately retrieve the phase in the sample by XRD with an angle of 10 °~ 80 ° and a

step length of 0.05 °. In Fig. 12(b), 1-Quartz (SiO_2), 2-Calcite (CaO), 3-Ca_3SiO_5, Ca_2SiO_3, 4-CSH. Quartz content is the highest, mainly because the coarse and fine aggregates are quartz and basalt, respectively. The two peaks of SiO_2 at 100 °C and 300 °C decrease tremendously, mainly because SiO_2 reacts with $Ca(OH)_2$, the hydration product of cement, to produce CSH (Eq.(10)). However, due to its amorphous structure, the peak value of CSH phase is low.[73] The rehydration corresponds to the increase of compressive strength of the sample in the previous Fig. 6. After 500 °C, the peak of SiO_2 increases and the peak of CSH decreases. This is mainly because most of CSH has decomposed to SiO_2 at 500 °C,[30] and the compressive strength decreases again. The peak of CaO increases significantly at 700 °C, indicating that the decarburization speed of $CaCO_3$ reaches a peak (Eq.(11)). CSH is almost completely decomposed at 700 °C, and the compressive strength of the sample in Fig. 6 decreases rapidly accordingly. C_nS (C_2S and C_3S) is also the decomposition product of CSH, and its peak value is low, but the peak values become more obvious at 700 °C and 900 °C. The synthesis and decomposition of the above phases correspond to the change of compressive strength of the sample after high temperature, that is, the compressive strength increases before 300 °C, and decreases after 500 °C.

$$3CaO \cdot SiO_2 + 2CaO \cdot SiO_2 + SiO_2 + H_2O \leftrightarrow xCaO \cdot ySiO_2 \cdot nH_2O(CSH) \tag{10}$$

$$CaCO_3 \leftrightarrow CaO + CO_2 \tag{11}$$

5 High-temperature pore characteristics related to macro compressive strength

5.1 Pore distribution characteristics

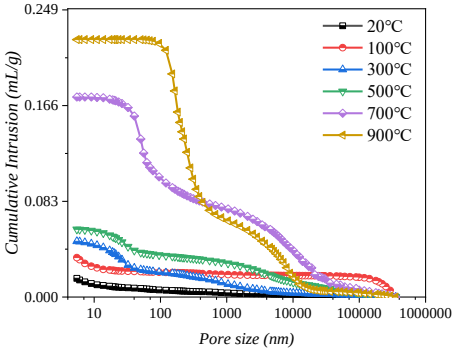

Fig. 13 Cumulative intrusion vs pore size after different temperatures

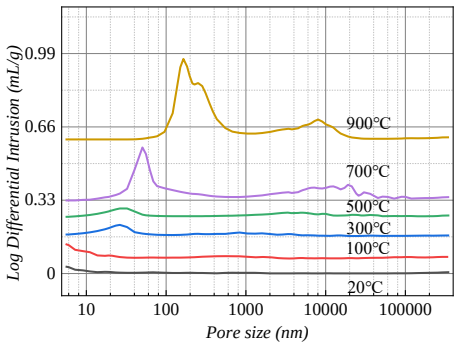

Fig. 14 Log differential intrusion vs pore size after different temperatures

A representative unit is cut from the middle of the sample for MIP testing. The type of automatic mercury intrusion porosimeter is AutoPore IV 9500, and the measuring range of holes is 5 nm ~ 350 μm. Fig. 13 shows the relationship between the cumulative intrusion and pore size of the CA-UHPC after different temperatures. It can be seen that from room temperature to 900 °C, the cumulative intrusion increases with the increase of temperature, basically showing a positive correlation. It is not difficult to find that the cumulative intrusion of the samples after 700 °C exhibits a huge growth, which is one order of magnitude larger than that of other temperatures. This implies that the internal pores of the material sharply grow after 700 °C, which result in a substantial reduction in mechanical properties, and is consistent with the sharp reduction of compressive strength in Fig. 6.

The critical diameter is often used to detect the influence of temperature on the change of pore structure. It is the inflection point of the cumulative intrusion curve (Fig. 13) and the maximum peak on the log differential intrusion curve (Fig. 14). The log differential intrusion curve is derived by differentiating the cumulative intrusion curve. In Fig. 14, the critical diameter constantly moves to the right, demonstrating that the internal pores of the CA-UHPC are coarsened by high temperature and larger pores are formed. To be specific, the critical diameter of the samples varies little from room temperature to 100 °C, and the peak value increases slightly. It is speculated that at 100 °C, the evaporation of free water leaves pores, while at the same time the rehydrated hydrate fills the pores. When the temperature continues to rise to between 300 °C and 500 °C, the critical diameter increases, indicating that, while some pores in the material have begun to coarsen, the pore size is still

relatively uniform. The internal pores continued to coarsen after 500 °C, and tended to form the second peak between 1000 nm and 10000 nm. At 700 °C and 900 °C, the critical diameter of internal pores moves to the right greatly, and the pore size is relatively concentrated, forming evident double peaks on the curve, and the pore size distribution is no longer uniform.

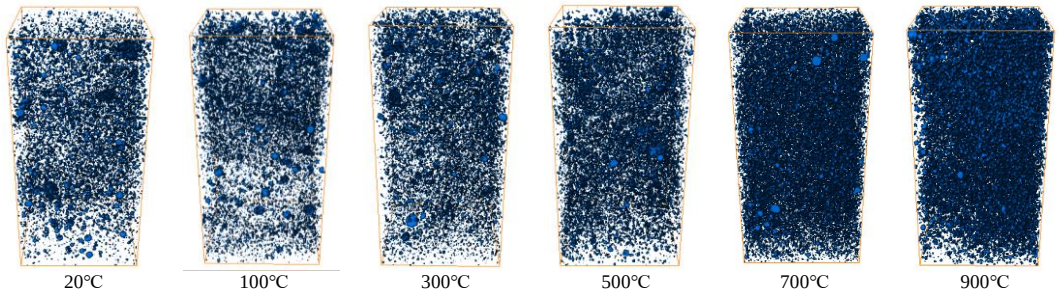

(a) 3D pore distribution

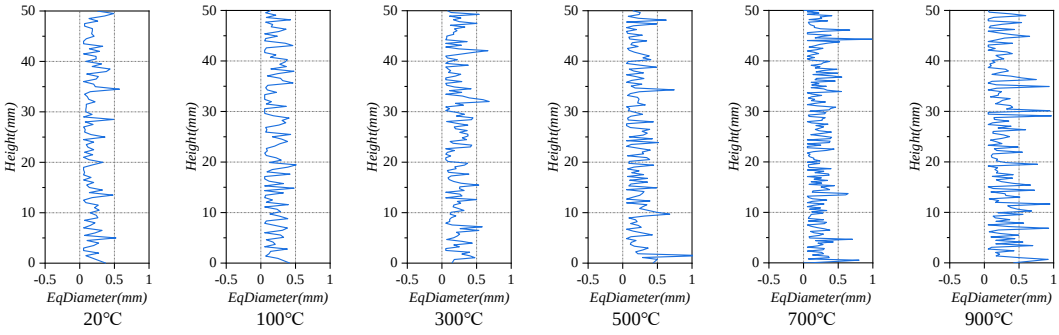

(b) Distribution of pores along height

Fig. 15 Pore distribution of 3D reconstructed CA-UHPC after different temperatures

X-CT can measure open and closed pores at the same time. The industrial X-CT (type: MultiscaleVoxel-450) with the pore recognition ability of Φ 200 μm is used. For the same sample as MIP, the pore distribution characteristics of three-dimensional reconstructed CA-UHPC by X-CT are shown in Fig. 15. From the figure, the total porosity tends to be larger as the temperature rises, as shown in Fig. 15 (a), and in Fig. 15 (b) as the larger area enclosed by the blue curve and the vertical axis (x=0). The distribution of the equivalent diameter along the height of the sample is not uniform either. More precisely, the porosity increases slightly from room temperature to 300 °C, in which the maximum diameter decreases at 100 °C and increases at 300 °C, but the median diameter is the smallest at 300 °C (see Fig. 17). The porosity continues to rise after 500 °C, and the porosity and the number of large pores significantly increase at 900 °C.

5.2 Porosity

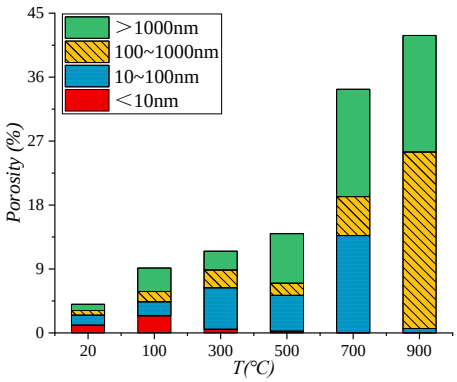

Fig. 16 Porosity and pore size distribution by MIP

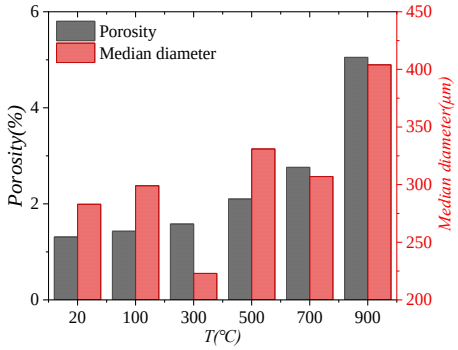

Fig. 17 Porosity and median diameter by X-CT

The porosity of the sample after exposed to different temperatures is shown in Fig. 16. The porosity is particularly sensitive to temperature and increases with the increase of temperature. Especially for the samples at 700 °C, the porosity increases sharply. However, the porosity is relatively stable at 700 °C ~900 °C. Samples exposed to different temperatures can be divided into three groups according to the porosity. The first is the

sample at room temperature, the porosity of which is less than 5%. The second is the sample at 100 °C ~ 500 °C that has a porosity between 8% ~ 20%. This group has a higher porosity than the first group, but with a slower pore growth rate. The compressive strength (Fig. 6) of the second group reduces up to 28%. The last group is the sample at 700 °C and 900 °C, the porosity of which is between 30% ~ 50%. In contrast with the previous group, the porosity increases significantly, and the compressive strength decreases rapidly, up to 78%. To further observe the pore characteristics [74], the pores are divided into macropores (d> 1000 nm), capillary pores (100 nm ＜d＜ 1000 nm), transition pores (10 nm ＜d＜ 100 nm) and gel pores (d< 10 nm), as shown in Fig. 16. After 100 °C, the number of pores increases, and there is little change in the proportion of different types of pores. At 300 °C, most part of the gel pores transforms into transition pores and the number of macropores decreases. Note here that the reduction of macropores means that the rehydration inside the structure fills part of the macropores and increases the compressive strength of the sample at this temperature. At 500 °C, the proportion of macropores increases to 50%, resulting in a decrease of compressive strength at 500 °C compared with 300 °C. At 700 °C and 900 °C, the total porosity increased noticeably, and gel pores could hardly be observed. At 900 °C, the number of large pores changes little compared with 700 °C, while most transition pores turn into capillary pores, and the compressive strength decreases further.

As can be seen from above, the porosity measured by MIP (Fig. 16) differs from that by X-CT (Fig. 17), because the range of the diameter measured by both methods is different. The sample used for MIP is small, generally 1mm ~ 5mm, and the measurement diameter is 5nm ~ 350 μm. Hence, MIP is better for identifying open pores at the nano level. While the resolution of X-CT is 50 μm, it is generally used to identify large pores (> 200) μm). In addition, the particle diameter of silica fume in the CA-UHPC is 0.2 μm, and the particle diameter of fly ash and cement is smaller than 150 μm. The number of large pores is relatively lower, so that the porosity identified by X-CT is smaller than that by MIP. Nevertheless, the porosity obtained by X-CT (Fig. 17) also shows increased with the increase of temperature. More specifically, from room temperature to 100 °C, the porosity and the median diameter increase, but not significantly. The temperature up to 100 °C has little effect on the compressive strength. Up to 300 °C, the porosity increases slightly, but the median diameter is smaller than that below 100 °C, which explains the increase of compressive strength at this temperature. After 500 °C, the porosity and the median diameter increase notably, and the compressive strength decreased greatly. The porosity increases while the median pore size decreases slightly at 700 °C. The porosity increases considerably at 900 °C, and the compressive strength decreases the most at this temperature.

6 Conclusion

This paper studied the change of mechanical properties and the micro structure evolution of CA-UHPC when the material was under and after exposure to high temperature, aiming at assessing the change of the temperature dependent macro strength of CA-UHPC and understanding the macro and micro thermal mechanisms that have caused the changes. The followings are the main findings.

(1) The macro morphological characteristics of CA-UHPC are greatly affected by a temperature higher than 300 °C, demonstrated by the changes in the color (from dark to light), knocking sound (from clear to dull), pore structures and crack formations (from small to large). The appearances featured by the CA-UHPC under or after heating are related to the maximum temperature exposed. Thus, the maximum temperature a CA-UHPC has experienced in a real fire can be evaluated according to the above macro morphological characteristics.

(2) Brittle failure characteristics of the CA-UHPC at hot and residual tests are noticeable below 500 °C. Volume distortion of the samples is obvious when the temperature reached 900 °C. The post-heating compressive strength is greater than the compressive strength of the same material exposed to high temperature. The coarse aggregate content is positively correlated with the high-temperature compressive strength, especially when the coarse aggregate content is about 30%. The shape of the test sample also has a certain effect on the compressive strength. The compressive strength of cubes is greater than that of prisms at the same temperature.

(3) The changes of macro and micro mass, morphology and phase after high temperature are closely related to the internal physicochemical changes of the CA-UHPC. The observed key stages are: (a) at 300 °C total loss of free water and rehydration occurs; (b) at 500 °C loss of all physically bound water and decomposition of CSH occur; (c) below 700 °C, change of quartz phase occurs, and the decomposition of CSH reaches the peak; (d) after 700 °C, the calcium carbonate decarburizes and all chemical bound water is lost. These micro structural and phase changes are directly related to changes in the macro compressive strength and can be used to assess high-temperature related strength degradation of CA-UHPC.

(4) A combination of both MIP and X-CT tests can provide a full account of pore characteristics of CA-UHPC at high-temperature, which can be also used to explain the reduction in high-temperature compressive strength. When the temperature is below 300 °C, although the porosity increases slightly, the median diameter of pores is the smallest, which corresponds to a slight increase in compressive strength. The number and size of the internal pores in the material sharply grow after 700 °C, resulting in a rapid reduction in compressive strength.

(5) In view of the correlations between strength degradation of CA-UHPC and high temperature, it is recommended that the service temperature of CA-UHPC should not excess 300 °C, so as to better maintain its strength without excessive property degradation. If the service temperature exceeds 700 °C, the compressive strength of CA-UHPC under and after heating is significantly reduced.

CRediT authorship contribution statement

Congcong Xue: Investigation, Formal analysis, Writing – original draft. **Min Yu:** Supervision, Project administration, Funding acquisition. **Haoming Xu:** Test, Data curation, Investigation. **Lihua Xu:** Funding acquisition, Resources. **Mohamed Saafi:** Supervision. **Jianqiao Ye:** Writing – review & editing, Supervision.

Acknowledgement

The authors are grateful for the financial support from the National Natural Science Foundation of China (Grant No. 51878518, 51738011), and China Scholarship Council (202006270175).

References

[1] Asadi I, Shafigh P, Hassan Z F B A, et al. Thermal Conductivity of Concrete– a Review[J]. Journal of Building Engineering, 2018:81-93.

[2] Wang H, Shi F, Shen J, et al. Research on the Self-Sensing and Mechanical Properties of Aligned Stainless Steel Fiber-Reinforced Reactive Powder Concrete[J]. Cement and Concrete Composites, 2021,119:104001.

[3] Shen L, Ding M, Chen K, et al. The Mechanical Behavior of RPC Under Combined Shear and Compressive Loads[J]. Cement and Concrete Composites, 2021,121:104071.

[4] Amin M, Zeyad A M, Tayeh B A, et al. Effects of Nano Cotton Stalk and Palm Leaf Ashes on Ultrahigh-Performance Concrete Properties Incorporating Recycled Concrete Aggregates[J]. Construction and Building Materials, 2021,302:124196.

[5] Amin M, Zeyad A M, Tayeh B A, et al. Effect of Ferrosilicon and Silica Fume on Mechanical, Durability, and Microstructure Characteristics of Ultra High-Performance Concrete[J]. Construction and Building Materials, 2022,320:126233.

[6] Wu F, Xu L, Chi Y, et al. Compressive and Flexural Properties of Ultra-High Performance Fiber-Reinforced Cementitious Composite: The Effect of Coarse Aggregate[J]. Composite Structures, 2020,236:111810.
[7] Amin M, Tayeh B A, Agwa I S. Effect of Using Mineral Admixtures and Ceramic Wastes as Coarse Aggregates on Properties of Ultrahigh-Performance Concrete[J]. Journal of Cleaner Production, 2020,273:123073.
[8] Roberti F, Cesari V F, de Matos P R, et al. High- and Ultra-High-Performance Concrete Produced with Sulfate-Resisting Cement and Steel Microfiber: Autogenous Shrinkage, Fresh-State, Mechanical Properties and Microstructure Characterization[J]. Construction and Building Materials, 2021,268:121092.
[9] Pyo S, Kim H, Lee B Y. Effects of Coarser Fine Aggregate on Tensile Properties of Ultra High Performance Concrete[J]. Cement and Concrete Composites, 2017,84:28-35.
[10] Yang J, Peng G, Zhao J, et al. On the Explosive Spalling Behavior of Ultra-High Performance Concrete with and without Coarse Aggregate Exposed to High Temperature[J]. Construction and Building Materials, 2019,226:932-944.
[11] Dauriac C. Special Concrete May Give Steel Stiff Competition[J]. The Seattle Daily Journal of Commerce, 1997,9:15-17.
[12] Du J, Meng W, Khayat K H, et al. New Development of Ultra-High-Performance Concrete (UHPC)[J]. Composites Part B: Engineering, 2021:109220.
[13] Bajaber M A, Hakeem I Y. UHPC Evolution, Development, and Utilization in Construction: A Review[J]. Journal of Materials Research and Technology, 2021,10:1058-1074.
[14] Shaikh F U A, Luhar S, Arel H ^, et al. Performance Evaluation of Ultrahigh Performance Fibre Reinforced Concrete – a Review[J]. Construction and Building Materials, 2020,232:117152.
[15] Ma Q, Guo R, Zhao Z, et al. Mechanical Properties of Concrete at High Temperature—a Review[J]. Construction and Building Materials, 2015,93:371-383.
[16] Li M, Qian C, Sun W. Mechanical Properties of High-Strength Concrete after Fire[J]. Cement and Concrete Research, 2004,34(6):1001-1005.
[17] Varona F B, Baeza F J, Bru D, et al. Influence of High Temperature on the Mechanical Properties of Hybrid Fibre Reinforced Normal and High Strength Concrete[J]. Construction and Building Materials, 2018,159:73-82.
[18] Kalifaa P, Chene G, Galle C. High-Temperature Behaviour of HPC with Polypropylene Fibres - From Spalling to Microstructure[J]. Cement and Concrete Research, 2001,31(10):1487-1499.
[19] Zhu Y, Hussein H, Kumar A, et al. A Review: Material and Structural Properties of UHPC at Elevated Temperatures or Fire Conditions[J]. Cement and Concrete Composites, 2021,123:104212.
[20] Wu H, Lin X, Zhou A. A Review of Mechanical Properties of Fibre Reinforced Concrete at Elevated Temperatures[J]. Cement and Concrete Research, 2020,135:106117.
[21] Li L, Khan M, Bai C, et al. Uniaxial Tensile Behavior, Flexural Properties, Empirical Calculation and Microstructure of Multi-Scale Fiber Reinforced Cement-Based Material at Elevated Temperature[J]. Materials, 2021,14(8):1827.
[22] Varona F B, Baeza F J, Bru D, et al. Influence of High Temperature on the Mechanical Properties of Hybrid Fibre Reinforced Normal and High Strength Concrete[J]. Construction and Building Materials, 2018,159:73-82.
[23] Tai Y, Pan H, Kung Y. Mechanical Properties of Steel Fiber Reinforced Reactive Powder Concrete Following Exposure to High Temperature Reaching 800°C[J]. Nuclear Engineering and Design, 2011,241(7):2416-2424.
[24] Zheng W, Li H, Wang Y. Compressive Behaviour of Hybrid Fiber-Reinforced Reactive Powder Concrete after High Temperature[J]. Materials & Design, 2012,41:403-409.

[25] Zheng W, Li H, Wang Y. Mechanical Properties of Reactive Powder Concrete with Different Dosage of Polypropylene Fiber after High Temperature[J]. Journal of Building Structures, 2012,33(9):119-126.
[26] Zheng W, Li H, Wang Y. Compressive Stress–Strain Relationship of Steel Fiber-Reinforced Reactive Powder Concrete after Exposure to Elevated Temperatures[J]. Construction and Building Materials, 2012,35:931-940.
[27] Zheng W, Luo B, Wang Y. Compressive and Tensile Properties of Reactive Powder Concrete with Steel Fibres at Elevated Temperatures[J]. Construction and Building Materials, 2013,41:844-851.
[28] Abid M, Hou X, Zheng W, et al. High Temperature and Residual Properties of Reactive Powder Concrete – a Review[J]. Construction and Building Materials, 2017,147:339-351.
[29] Abid M, Hou X, Zheng W, et al. Mechanical Properties of Steel Fiber-Reinforced Reactive Powder Concrete at High Temperature and after Cooling[J]. Procedia Engineering, 2017,210:597-604.
[30] Abid M, Hou X, Zheng W, et al. Effect of Fibers on High-Temperature Mechanical Behavior and Microstructure of Reactive Powder Concrete[J]. Materials, 2019,12(2):329.
[31] Sanchayan S, Foster S J. High Temperature Behaviour of Hybrid Steel–PVA Fibre Reinforced Reactive Powder Concrete[J]. Materials and Structures, 2016,49(3):769-782.
[32] Siemon M, Zehfuß J. Experimental and Numerical Analysis of Ultra High Performance Concrete (UHPC) Members in Case of Fire[J]. Applications of Structural Fire Engineering, 2016.
[33] Banerji S, Kodur V. Effect of Temperature on Mechanical Properties of Ultra-High Performance Concrete[J]. Fire and Materials, 2021,46.
[34] Ahmad S, Rasul M, Adekunle S K, et al. Mechanical Properties of Steel Fiber-Reinforced UHPC Mixtures Exposed to Elevated Temperature: Effects of Exposure Duration and Fiber Content[J]. Composites Part B: Engineering, 2019,168:291-301.
[35] Shen W, Liu Y, Cao L, et al. Mixing Design and Microstructure of Ultra High Strength Concrete with Manufactured Sand[J]. Construction and Building Materials, 2017,143:312-321.
[36] Kim K Y, Yun T S, Park K P. Evaluation of Pore Structures and Cracking in Cement Paste Exposed to Elevated Temperatures by X-Ray Computed Tomography[J]. Cement and Concrete Research, 2013,50:34-40.
[37] Lee N K, Koh K T, Park S H, et al. Microstructural Investigation of Calcium Aluminate Cement-Based Ultra-High Performance Concrete (UHPC) Exposed to High Temperatures[J]. Cement and Concrete Research, 2017,102:109-118.
[38] Seo J, Bae S J, Jang D I, et al. Thermal Behavior of Alkali-Activated Fly Ash/Slag with the Addition of an Aerogel as an Aggregate Replacement[J]. Cement and Concrete Composites, 2020,106:103462.
[39] Canbaz M. The Effect of High Temperature on Reactive Powder Concrete[J]. Construction and Building Materials, 2014,70:508-513.
[40] Abdul-Rahman M, Al-Attar A A, Hamada H M, et al. Microstructure and Structural Analysis of Polypropylene Fibre Reinforced Reactive Powder Concrete Beams Exposed to Elevated Temperature[J]. Journal of Building Engineering, 2020,29:101167.
[41] Alyaa A. A, Mazin B. A, Hussein M. H, et al. Investigating the Behaviour of Hybrid Fibre-Reinforced Reactive Powder Concrete Beams after Exposure to Elevated Temperatures[J]. Journal of Materials Research and Technology, 2020,9(2):1966-1977.
[42] Baharuddin N K, Nazri F M, Bakar B H A, et al. Potential Use of Ultra High-Performance Fibre-Reinforced Concrete as a Repair Material for Fire-Damaged Concrete in Terms of Bond Strength[J]. International Journal of Integrated Engineering, 2020,12(9):87-95.
[43] Sollero M B S, Moreno Junior A L, Costa C N. Residual Mechanical Strength of Concrete Exposed to High Temperatures – International Standardization and Influence of Coarse Aggregates[J]. Construction and Building Materials, 2021,287:122843.

[44] Lau A, Anson M. Effect of High Temperatures on High Performance Steel Fibre Reinforced Concrete[J]. Cement and Concrete Research, 2006,36(9):1698-1707.
[45] Collepardi S, Coppola L, Troli R. Mechanical Properties of Modified Reactive Powder Concrete[J]. Journal of optoelectronics & advanced materials, 1997.
[46] Wang C, Yang C, Liu F, et al. Preparation of Ultra-High Performance Concrete with Common Technology and Materials[J]. Cement and Concrete Composites, 2012,34(4):538-544.
[47] Deng F, Xu L, Chi Y, et al. Effect of Steel-Polypropylene Hybrid Fiber and Coarse Aggregate Inclusion on the Stress–Strain Behavior of Ultra-High Performance Concrete Under Uniaxial Compression[J]. Composite Structures, 2020,252:112685.
[48] Li L, Xu L, Huang L, et al. Compressive Fatigue Behaviors of Ultra-High Performance Concrete Containing Coarse Aggregate[J]. Cement and Concrete Composites, 2022,128:104425.
[49] Ultra High Performance Fibre-Reinforced Concretes Recommendations[S]. AFGC SETRA Working Group, Paris, France, 2013.
[50] ASTM C1856M-17 Standard Practice for Fabricating and Testing Specimens of Ultra-High Performance Concrete[S]. ASTM International, 2017.
[51] GB/T 31387-2015 Reactive Powder Concrete. Beijing, China; 2015.
[52] T/CECS 10107-2020 Technical Requirements for Ultra High Performance Concrete (UHPC). Beijing, China; 2020.
[53] Perry V H. What Really is Ultra-High Performance Concrete -Towards a Global Definition [C]. The 2nd Int. Conference on Ultra-High Performance Concrete Material & Structures, Fuzhou, China, 2018.
[54] Zhu Y, Hussein H, Kumar A, et al. A Review: Material and Structural Properties of UHPC at Elevated Temperatures or Fire Conditions[J]. Cement and Concrete Composites, 2021,123:104212.
[55] Xue C, Yu M, Xu H, et al. Experimental Study on Thermal Performance of Ultra-High Performance Concrete with Coarse Aggregates at High Temperature[J]. Construction and Building Materials, 2022,314:125585.
[56] Amin M, Tayeh B A, Agwa I S. Investigating the Mechanical and Microstructure Properties of Fibre-Reinforced Lightweight Concrete under Elevated Temperatures[J]. Case Studies in Construction Materials, 2020,13:e459.
[57] Amin M, Hakeem I Y, Zeyad A M, et al. Influence of Recycled Aggregates and Carbon Nanofibres on Properties of Ultra-High-Performance Concrete under Elevated Temperatures[J]. Case Studies in Construction Materials, 2022,16:e1063.
[58] Zhang Y, Sun Q, Yang X. Changes in Color and Thermal Properties of Fly Ash Cement Mortar after Heat Treatment[J]. Construction and Building Materials, 2018,165:72-81.
[59] Short N R, Purkiss J A, Guise S E. Assessment of Fire Damaged Concrete Using Colour Image Analysis[J]. Construction and Building Materials, 2001,15(1):9-15.
[60] Tobbala D E, Abdelsalam B A, Agwa I S. Bond Performance of a Hybrid Coating Zinc-Rich Epoxy Incorporating Nano-Ferrite for Steel Rebars Subjected to High Temperatures in Concrete[J]. Journal of Building Engineering, 2020,32:101698.
[61] Mehta P K, Monteiro P J M. Concrete: Structure, Properties and Materials.2Nd Ed[M]. New Jersey: Prentice Hall International: 2013.
[62] Fu Y, Wong Y, Poon C, et al. Experimental Study of Micro/Macro Crack Development and Stress–Strain Relations of Cement-Based Composite Materials at Elevated Temperatures[J]. Cement and Concrete Research, 2004,34(5):789-797.
[63] Nam J, Yun J, Song Y, et al. Analysis of Influence Factors to Compressive and Tensile Strength of Basalt in Cheju Island[J]. The Journal of Engineering Geology, 2008,18(2):215-225.
[64] So H, Jang H, Khulgadai J, et al. Mechanical Properties and Microstructure of Reactive Powder Concrete Using Ternary Pozzolanic Materials at Elevated Temperature[J]. Ksce Journal of Civil

Engineering, 2015,19(4):1050-1057.
[65] Tang J, Ma W, Pang Y, et al. Uniaxial Compression Performance and Stress–Strain Constitutive Model of the Aluminate Cement-Based UHPC after High Temperature[J]. Construction and Building Materials, 2021,309:125173.
[66] W Zheng, H Li, Y Wang. Mechanical Properties of Reactive Powder Concrete with Different Dosage of Polypropylene Fiber after High Temperature[J]. Journal of Building Structures, 2012,33(09):119-126.
[67] Xiong M, Liew J Y R. Spalling Behavior and Residual Resistance of Fibre Reinforced Ultra-High Performance Concrete after Exposure to High Temperatures[J]. Materiales De Construccion, 2015,65(320).
[68] Xiong M, Liew J Y R. Mechanical Behaviour of Ultra-High Strength Concrete at Elevated Temperatures and Fire Resistance of Ultra-High Strength Concrete Filled Steel Tubes[J]. Materials & Design, 2016,104:414-427.
[69] Choe G, Kim G, Gucunski N, et al. Evaluation of the Mechanical Properties of 200 MPa Ultra-High-Strength Concrete at Elevated Temperatures and Residual Strength of Column[J]. Construction and Building Materials, 2015,86:159-168.
[70] Myers R J, L'Hôpital E, Provis J L, et al. Effect of Temperature and Aluminium on Calcium (Alumino)Silicate Hydrate Chemistry Under Equilibrium Conditions[J]. Cement and Concrete Research, 2015,68:83-93.
[71] Akca A H, özyurt N. Effects of Re-Curing on Microstructure of Concrete after High Temperature Exposure[J]. Construction and Building Materials, 2018,168:431-441.
[72] Kim J, Lee G, Moon D Y. Evaluation of Mechanical Properties of Steel-Fibre-Reinforced Concrete Exposed to High Temperatures by Double-Punch Test[J]. Construction and Building Materials, 2015,79:182-191.
[73] Caetano H, Ferreira G, Rodrigues J P C, et al. Effect of the High Temperatures on the Microstructure and Compressive Strength of High Strength Fibre Concretes[J]. Construction and Building Materials, 2019,199:717-736.
[74] Jin S, Zhang J, Han S. Fractal Analysis of Relation Between Strength and Pore Structure of Hardened Mortar[J]. Construction and Building Materials, 2017,135:1-7.